

Engineering quantum spin Hall state in semiconducting transition metal dichalcogenide monolayer by alloying with Os

Liying Ouyang, Can Qi, and Jun Hu*

*School of Physics and Technology, Soochow University, Suzhou, Jiangsu 215006, China.
Jiangsu Key Laboratory of Thin Films, Soochow University, Suzhou, Jiangsu 215006, China.*

Exploring topological phases in two-dimensional (2D) semiconductors which are ready in experiment may facilitate the research on 2D topological insulators. Through first-principles and tight-binding simulations, we proposed an effective way to produce quantum spin Hall (QSH) states in 2D Mo and W dichalcogenide monolayers by alloying with Os. Analysis of electronic structures reveals that the QSH states originate mainly from the 5d orbitals of the Os atom. These orbitals possess large spin–orbit coupling constant, so that the QSH gaps are notably large (~ 30 meV) and can be enhanced to 42.6 meV by compressive biaxial strain. Our study paves the way to engineer topological phases in 2D semiconductors.

I. INTRODUCTION

Topological insulator (TI) state, discovered in recent years, is a new state of condensed matter.^{1–8} It is characterized by the combination of insulating bulk state and quantized helical conducting edge state, which exhibits intriguing quantum spin Hall (QSH) effect. Here the helical state provides intrinsic spin lock localized at the edge and is robust against elastic backscattering, so it is ideal for various applications that require dissipationless spin transport.^{7,8} Although QSH state was firstly predicted in graphene which is an ideal two-dimensional (2D) material, it is difficult to observe it in graphene due to the weak intrinsic spin-orbit coupling (SOC).^{9–11} On the contrary, significant progress on the investigation of TIs in experiment was made in quantum wells^{4,6,12–14} and three-dimensional (3D) TIs^{15–19}. However, the transport properties of 3D TIs are more difficult to control than those of 2D TIs, due to the gapless side surface states in 3D TIs. Therefore, 2D TIs are more promising for practical applications, since the quantized helical states only exist at the edges of 2D TIs.

Many possible 2D TIs have been predicted in recent years,^{20–23} but very few of them were achieved in experiments, because most 2D TIs predicted in theories must be decorated by anion atoms (such as H and halogen elements) and kept away from substrate. However, it is difficult to grow free-standing 2D TIs in experiment. For example, freestanding silicene in honeycomb lattice was predicted to be TI with nontrivial gap of 1.55 meV, but the honeycomb silicene has been fabricated only on some transition metal surfaces such as Ag(111) and Ir(111).^{24–26} Unfortunately, there is no evidence yet that the honeycomb silicene on these transition metal surfaces still preserves the QSH state. Furthermore, large TI gaps are desired for possible applications of the 2D TIs at room temperature. Therefore, it is interesting and important to search for 2D TIs that not only have large TI gaps but also are feasible to fabricate.

Recently, the 2D transition metal dichalcogenide (TMD) monolayers have attracted great attention, because they exhibit versatile electronic properties yet are chemically and physically stable.^{27,28} Most importantly, the 2D TMD monolayers can be obtained easily either through exfoliation of bulk materials or bottom-up syntheses.^{29,30} In this family, the

2D molybdenum and tungsten dichalcogenide monolayers — MoX_2 and WX_2 ($\text{X} = \text{S, Se or Te}$) — are semiconductors with sizable band gaps $1 \sim 2$ eV and possess fascinating valleytronic character.³¹ Interestingly, QSH states were predicted in 2D MoX_2 and WX_2 monolayers with either structural distortion³² or metastable phase³³. These studies provide new opportunities to explore the QSH effect in semiconducting 2D materials.

Alloying with certain elements is an effective method to engineer the electronic property of materials,³⁴ which may induce intriguing feature such as dilute magnetism.³⁵ Therefore, it is possible to produce QSH states in 2D MoX_2 and WX_2 by alloying with exotic elements. Meanwhile, the QSH states are closely associated with the strength SOC, hence strong SOC is desired to achieve large TI gap. In this paper, we investigated the electronic properties of 2D MoX_2 and WX_2 alloyed with 5d transition metal elements, through first-principles calculations and tight-binding modeling. We found that Os is a good candidate to turn MoX_2 and WTe_2 into TIs, with nontrivial band gaps ranging from 5.3 meV to 32.3 meV. Moreover, the TI gaps can be tuned by external strain.

II. COMPUTATIONAL DETAILS

The structural and electronic properties were calculated with density functional theory (DFT) as implemented in the Vienna *ab-initio* simulation package.^{36,37} The interaction between valence electrons and ionic cores was described within the framework of the projector augmented wave (PAW) method.^{38,39} The generalized gradient approximation (GGA) was used for the exchange-correlation potentials and the SOC effect was invoked self-consistently.⁴⁰ The energy cutoff for the plane wave basis expansion was set to 500 eV. A 2×2 supercell was employed and the 2D Brillouin zone was sampled by a 27×27 k-grid mesh. The atomic positions were fully relaxed with a criterion that requires the forces on each atom smaller than 0.01 eV/Å. To determine the topological character of the considered system, we employed the n –field method to calculate the topological invariant \mathbb{Z}_2 .^{42–44} The band structures of one-dimensional (1D) nanoribbons were calculated by the tight-binding model⁴⁵ based on the maximally localized Wannier functions (MLWFs)^{46,47} as imple-

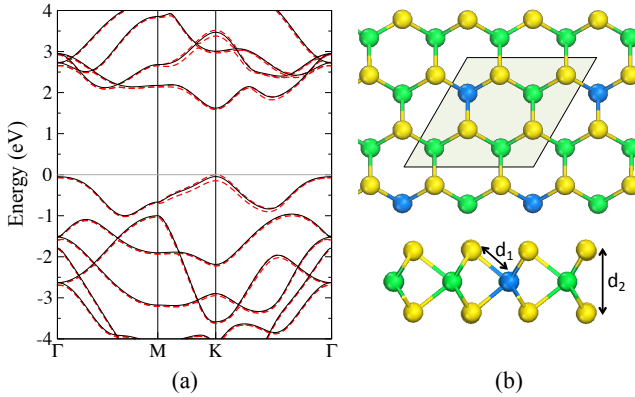


FIG. 1. (Color online) (a) Band structure of pure MoS₂ monolayer without (black solid curves) and with (red dashed curves) SOC. The grey horizontal line indicates the Fermi level. (b) Top and side views of the Os alloyed MX₂ (M = Mo, W; X = S, Se, Te) monolayer. The purple, blue and green balls represent Os, M and X atoms. The rhombus represent the unit cell which is the 2 \times 2 supercell of pure MX₂ with one M atom replace by the Os atom.

mented in the Wannier90 code.⁴⁸

III. RESULTS AND DISCUSSION

We firstly optimized the lattice constants and calculated the band structures of the Mo and W dichalcogenide monolayers. As listed in Table I, the lattice constants are slightly larger than those of their bulk counterparts²⁷ but in agreement with previous calculations.⁴⁹ In addition, they increase as the anion changes from S to Te owing to the increasing atomic radii of the anions. However, the lattice constants do not differ visibly for MoX₂ and WX₂ monolayers with the same anion element. Therefore, it is convenient to fabricate alloyed Mo_{1-x}W_xX₂ monolayers with the intentional concentration of Mo or W to adjust the SOC strength, electronic and chemical properties.^{50,51}

All MoX₂ and WX₂ monolayers are semiconductors with sizable band gaps (E_g) as seen in Table I. Furthermore, the gaps undergo an indirect to direct transition from the bulk phase to monolayer form.^{27,29} For example, the bulk MoS₂ has an indirect E_g of 1.2 eV, while the E_g of the MoS₂ monolayer is 1.8 eV, due to the quantum confinement in monolayer.²⁹ From Table I, it can be seen that the calculated E_g of MoS₂ monolayer is 1.59 eV, smaller than the experimental value. This is caused by the well known problem that GGA calcula-

TABLE I. The band gaps (E_g , in eV) and lattice constants (a , in Å) of pure MX₂ (M = Mo, W; X = S, Se, Te) monolayers. The SOC has been involved.

	Mo			W		
	S	Se	Te	S	Se	Te
a	3.19	3.33	3.56	3.19	3.33	3.56
E_g	1.59	1.31	0.94	1.53	1.24	0.75

TABLE II. The lattice constants (a , in Å), global and direct band gaps (E_g and E'_g , in eV) and \mathbb{Z}_2 invariant of Os alloyed MX₂ (M = Mo, W; X = S, Se, Te) monolayers. The SOC has been involved.

	Mo			W		
	S	Se	Te	S	Se	Te
a	6.50	6.78	7.27	6.48	6.78	7.26
E_g	32.3	31.8	25.4	-	-	5.3
E'_g	37.4	31.8	25.4	29.6	8.8	5.3
\mathbb{Z}_2	1	1	1	-	-	1

tions underestimate band gaps of semiconductors. Nevertheless, the band structure plotted in Figure 1a capture the main electronic feature of the MoS₂ monolayer, that is, the MoS₂ monolayer is a direct-band-gap semiconductor with the valence band maximum (VBM) and conduction band minimum (CBM) locating at K point. In addition, the SOC effect results in splitting of the valence bands around the K point as well as $-K$ point. Owing to the time reversal symmetry, this splitting leads to fascinating valley Hall effect known as valleytronics in these monolayers.³¹

Then we choose MoS₂ as a prototype to investigate the effect of alloying on the electronic structures, by alloying with 5d transition metal elements. One of the Mo atoms in a 2x2 supercell is replaced by a 5d transition metal atom, resulting in an alloyed compound with Mo and 5d transition metal concentrations of 0.75 and 0.25, respectively, as shown in Figure 1b and 1c. After relaxation of lattice and atomic structures, we calculated the band structures of MoS₂ alloyed with 5d transition metal from Ta to Ir, as plotted in Figure S1 in the Supplementary Information. It is clear that alloying with W does not lead to visible change of the band structures, because MoS₂ and WS₂ have almost the same atomic structure and close band structure.^{50,51} Alloying with Ta, Re and Ir makes the new compounds metallic. Interestingly, Mo_{0.75}Os_{0.25}S₂ alloy shows a SOC induced band gap near the middle point of the path from Γ to K, which may be a signature of QSH states. Therefore, we focus on Os alloyed compounds in the following.

The optimized lattice constant of Mo_{0.75}Os_{0.25}S₂ alloy is listed in Table II, which expands by 19.3% compared to that of MoS₂. To explore the electronic property of this alloy, we plotted the atom-resolved band structure without including the SOC effect in Figure 2a. It can be seen that the Os atom hybridizes strongly with the host MoS₂, which induces two bands ('I' and 'II') in the gap of MoS₂. These bands become degenerate at the Γ point and restore atomic orbital character as represented by the corresponding local charge density in the inset of Figure 2. Clearly, the charge density has local C_{3v} symmetry around the Os atoms, and characterizes apparent in-plane components of the d orbitals (d_{xy} and $d_{x^2-y^2}$) of Mo and Os atoms. Note that the charge density around the Os atom has round shape, mainly due to the large sizes of the d_{xy} and $d_{x^2-y^2}$ orbitals which hybridize strongly with the S atoms. Accordingly, we sort the d orbitals into three groups: (i) d_{z^2} ; (ii) d_{xz} and d_{yz} ; and (iii) d_{xy} and $d_{x^2-y^2}$. The projections of these orbitals on the electronic bands are plotted in Figure 2b and 2c. We can see that the energy level at the

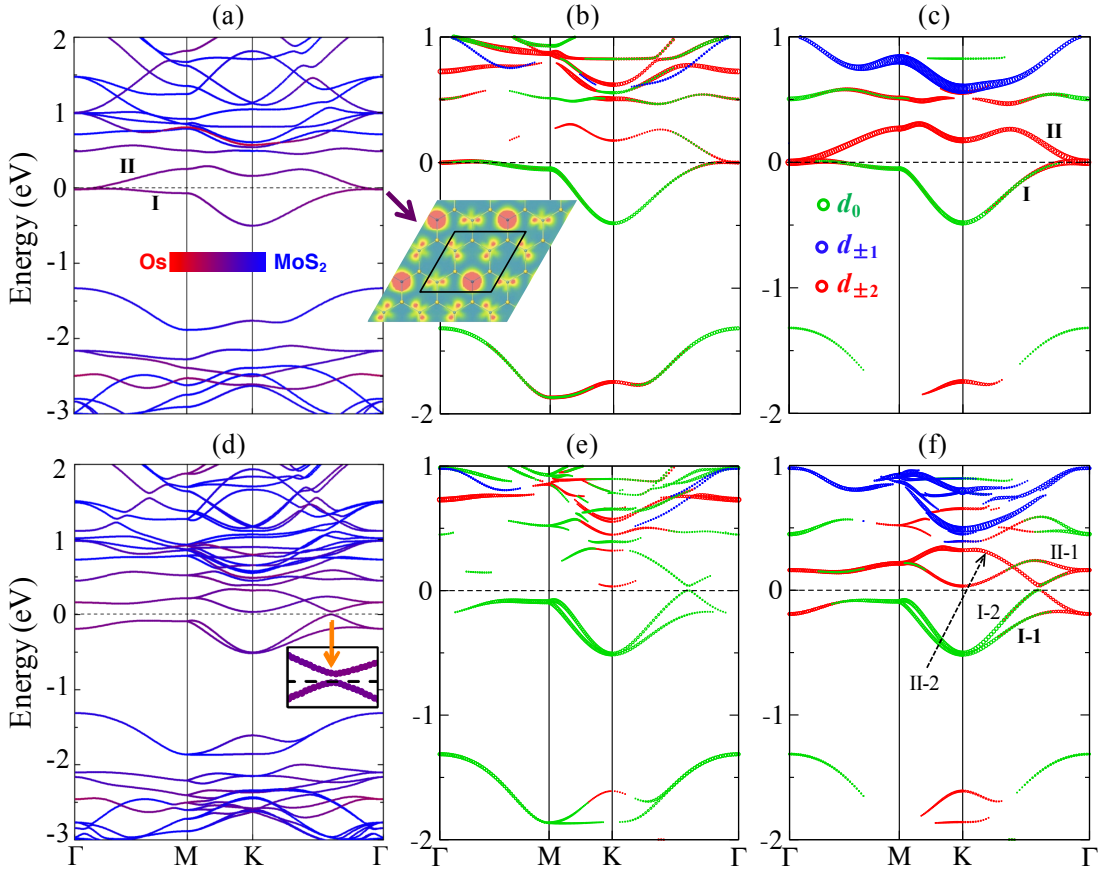


FIG. 2. (Color online) Band structures of $\text{Mo}_{0.75}\text{Os}_{0.25}\text{S}_2$ alloy without (a–c) and with (d–f) SOC. The horizontal dashed lines indicate the Fermi level. (a,d) Projection on Os and MoS_2 . The color bar represents the weight of the Os atom and the host MoO_2 . The pure red/blue color means no interaction, while intermediate purple color means strong interaction between Os and MoS_2 . (b,e) Projection on Mo 4d orbitals. (c,f) Projection on Os 5d orbitals. For simplicity, the d_{z^2} , $d_{xz/yz}$ and d_{xy/x^2-y^2} orbitals are notated as d_0 , $d_{\pm 1}$ and $d_{\pm 2}$, respectively. The sizes of the dots stand for the weights of the corresponding orbitals. The inset displays the charge density projected on the cation plane of the energy level at the E_F of the Γ point as indicated by the purple arrow. The yellow, light cyan and dark cyan spheres represent S, Mo and Os atoms, respectively.

E_F of the Γ point originates from the d_{xy/x^2-y^2} orbitals of both Mo and Os atoms and the weight of the Os atom is significantly larger than that of the Mo atom. As the bands propagate to the \mathbf{M} and \mathbf{K} points, the degeneracy at the Γ point breaks and the energy level evolves into two bands. The band ‘II’ goes upwards and keeps pure d_{xy/x^2-y^2} state which is dominated by the Os atom. The band ‘I’ goes downwards, with the weight of the d_{xy/x^2-y^2} orbitals decreasing and the weight of the d_{z^2} orbital increasing. Finally, the band ‘I’ near the \mathbf{K} point is contributed by the d_{z^2} orbital completely, and the weight of the Os atom is slightly larger than that of the Mo atom. For the $d_{xz/yz}$ orbitals, those of the Os atom contribute to the bands ~ 0.5 eV above the E_F , while those of the Mo atom do not have notable contribution to the bands within the energy range in Figure 2b. When the SOC effect is included, the degeneracy of the bands ‘I’ and ‘II’ at the Γ point is removed and a large gap of 0.45 eV opens, as shown in Figure 2d. Each of these bands further splits into two bands along the path of $\Gamma - \mathbf{K} - \mathbf{M}$. Interestingly, the band ‘I-2’ goes upwards faster than the band ‘I-1’ from \mathbf{K} to Γ , so it crosses the

E_F . At the same time, the band ‘II-2’ goes downwards and crosses the E_F at the same k point. As a consequence, band inversion occurs between the bands ‘I-2’ and ‘II-2’, i.e. the d_{z^2} and d_{xy/x^2-y^2} orbitals, which is a signature of nontrivial topological phase in this material.⁴ In addition, the bands ‘I-2’ and ‘II-2’ interact with each other through the SOC Hamiltonian, yielding a nontrivial gap of 37.4 meV. Note that the actual CBM (i.e. the minimum of the bands ‘II-1’ and ‘II-2’ as seen in Figure 2f) locates at \mathbf{K} point rather than the crossing point, which suggests that the global gap of $\text{Mo}_{0.75}\text{Os}_{0.25}\text{S}_2$ is actually an indirect band gap with a smaller amplitude of 32.3 meV. Furthermore, the E_F locates in this SOC induced gap. Accordingly, we can conclude that the $\text{Mo}_{0.75}\text{Os}_{0.25}\text{S}_2$ alloy is a natural TI which does not require the gate voltage to adjust the E_F . This is a good feature for both experimental investigations and practical applications.

The electronic band topology can be characterized by the \mathbb{Z}_2 invariant. So we calculated \mathbb{Z}_2 of the $\text{Mo}_{0.75}\text{Os}_{0.25}\text{S}_2$ alloy with the n –field method.^{42–44} By counting the positive and negative n –field numbers over half of the torus as indicated

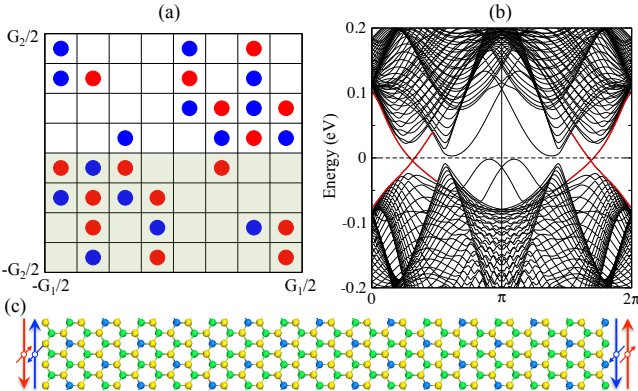


FIG. 3. (Color online) (a) The n -field configuration of $\text{Mo}_{0.75}\text{Os}_{0.25}\text{S}_2$. The nonzero points are denoted by red ($n = 1$) and blue ($n = -1$) dots, respectively. The \mathbb{Z}_2 invariant is obtained by summing the n -field over half Brillouin zone marked by the shadow. (b, c) Band structure and atomic structure of 1D $\text{Mo}_{0.75}\text{Os}_{0.25}\text{S}_2$ nanoribbon with zigzag edges. The actual width of the 1D nanoribbon in calculation is 30 unit cells (*u.c.*). The horizontal dashed line in (b) represents the Fermi level. The long arrows in (c) indicate the directions of the edge currents. The short arrows denote the spin-up (red) and spin-down (blue) electrons, respectively.

in Figure 3a, we obtained $\mathbb{Z}_2 = 1$ for the $\text{Mo}_{0.75}\text{Os}_{0.25}\text{S}_2$ alloy, clearly demonstrating the nontrivial band topology. In fact, the topological insulators are also manifested by quantized edge states which brings about the QSH effect.^{7,8} Therefore, we calculated the band structure of a 1D nanoribbon of $\text{Mo}_{0.75}\text{Os}_{0.25}\text{S}_2$ with zigzag edges and width of 30 unit cells, as plotted in Figure 3b and 3c. Apparently, linearly dispersive bands appear in the gap of the 2D $\text{Mo}_{0.75}\text{Os}_{0.25}\text{S}_2$ and their wave functions are localized at the edge regions of the nanoribbon. Consequently, these edge bands provide the helical edge states for the QSH effect.

For MoSe_2 and MoTe_2 , alloying with Os leads to lattice expansion similar to MoS_2 , as listed in Table II. The band structures before and after including the SOC effect are plotted in Figure 4. Clearly, the SOC has two effects on the electronic band structures. Firstly, it eliminates the degeneracy of the two bands beside the E_F at the Γ point; and secondly, it induces a nontrivial gap near the middle point of the path from Γ to \mathbf{K} for both $\text{Mo}_{0.75}\text{Os}_{0.25}\text{Se}_2$ and $\text{Mo}_{0.75}\text{Os}_{0.25}\text{Te}_2$, with amplitudes of 31.8 and 25.4 meV, respectively. Note that both gaps are direct band gaps, with the VBM and CBM at the same k point in the Brillouin zone. Interestingly, the \mathbb{Z}_2 invariant of both cases is 1, implying nontrivial band topology. The band structures of the 1D nanoribbons in Figure 4c and 4f demonstrate the existence of quantized edge states in the 1D nanoribbons. Therefore, the QSH states can be realized in the whole family of $\text{Mo}_{0.75}\text{Os}_{0.25}\text{X}_2$ ($\text{X} = \text{S}, \text{Se}$ and Te). On the other hand, for the family of $\text{W}_{0.75}\text{Os}_{0.25}\text{X}_2$, only $\text{W}_{0.75}\text{Os}_{0.25}\text{Te}_2$ is a TI with a nontrivial band gap of 5.3 meV and its 1D nanoribbon exhibits quantized edge states, as seen in Figure S2 and S3 in the Supplementary Information.

From table II, we can see that the direct band gaps of both $\text{Mo}_{0.75}\text{Os}_{0.25}\text{X}_2$ and $\text{W}_{0.75}\text{Os}_{0.25}\text{X}_2$ decrease as the

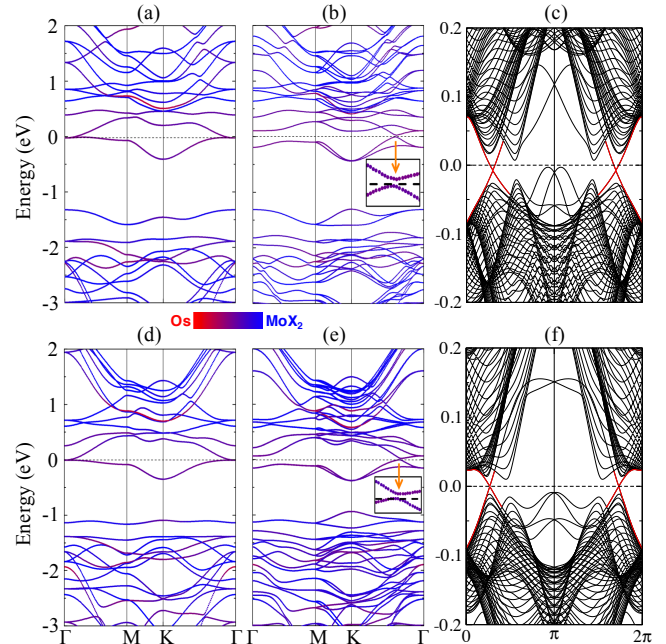


FIG. 4. (Color online) Band structures of Os alloyed MoSe_2 (a-c) and MoTe_2 (d-f). (a,d) and (b,e) are species-resolved band structures without and with SOC, respectively. (c,f) are band structures of 1D nanoribbon with zigzag edges. The actual width of the 1D nanoribbon in calculation is 30 unit cells (*u.c.*). The horizontal dashed line represents the Fermi level.

atomic sizes of the anions increase. This is because when the Os-X bond lengths increase, the interaction between the bands 'I-2' and 'II-2' weakens. Therefore, the band gap may be engineered by external strain, as indicated by the inset in Figure 5. We calculated the band structures of $\text{Mo}_{0.75}\text{Os}_{0.25}\text{X}_2$ alloys under biaxial strain from -2% to 4%, as plotted in Figure S4–S6 in the Supplementary Information. For all cases, the bands near the direct gaps undergo similar evolutions to that shown in the inset in Figure 5. The nontrivial band gaps decrease slightly under extensile strain while increase significantly under compressive strain. For $\text{Mo}_{0.75}\text{Os}_{0.25}\text{S}_2$, the compressive strain leads to metallic electronic property, although the nontrivial direct band gap increases. For $\text{Mo}_{0.75}\text{Os}_{0.25}\text{Se}_2$, a compressive strain of -1% turns the gap into indirect band gap (33.2 meV), slightly larger than that without strain. When the compressive strain increases to -2%, $\text{Mo}_{0.75}\text{Os}_{0.25}\text{Se}_2$ becomes metallic. The band gap of $\text{Mo}_{0.75}\text{Os}_{0.25}\text{Te}_2$ keeps direct under compressive strain up to -2% and increases to 42.6 meV, 1.7 times larger than that without strain (25.4 meV). Therefore, compressive strain is an effective way to engineer the nontrivial band gap of $\text{Mo}_{0.75}\text{Os}_{0.25}\text{Te}_2$.

IV. CONCLUSION

In summary, through systematic first-principles calculations and tight-binding modeling, we have found that alloy-

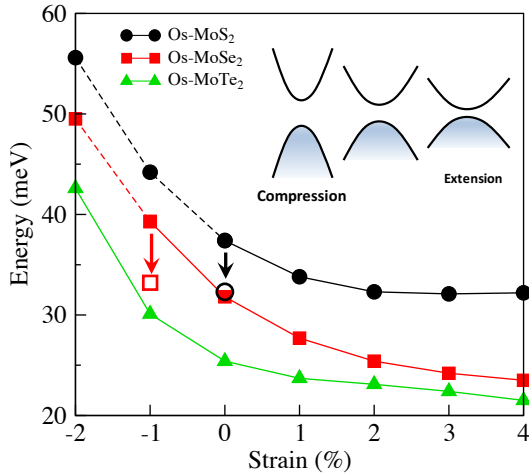


FIG. 5. (Color online) The nontrivial direct band gaps as a function of biaxial strain for $\text{Mo}_{0.75}\text{Os}_{0.25}\text{X}_2$ ($\text{X} = \text{S}, \text{Se}$ and Te). The strain is defined as $(a/a_0 - 1) \times 100\%$ with negative and positive values for compressive and extensile strains. a and a_0 are the lattice constants under and with external strain, respectively. The open square and circle stand for the indirect band gaps when they are smaller the corresponding direct band gaps as indicated by the arrows. The dashed lines indicate that the systems become metallic, although there are large direct band gaps. The inset shows the schematic band evolutions under compressive and extensile strains. The shadow areas indicate the occupied bands (valence bands).

ing the 2D MoX_2 and WX_2 monolayers with Os transforms them from semiconductors into TIs with sizable nontrivial band gaps ranging from 5.3 meV to 32.3 meV. The corresponding alloys have nonzero \mathbb{Z}_2 invariant and clear quantized edge states. Analysis of electronic structures reveals that band inversion occurs between the d_{z^2} and d_{xy/x^2-y^2} orbitals of the Os atom caused by the SOC effect. This band inversion plays the most important role in the QSH state. Interestingly, the TI gaps can be tuned by external biaxial strain. In particular, the TI gap of $\text{Mo}_{0.75}\text{Os}_{0.25}\text{Te}_2$ can vary from 42.6 eV to 21.5 meV for strain from -2% to 4%. Our study paves the way to engineer QSH states in 2D semiconductors.

ACKNOWLEDGEMENTS

This work is supported by the National Natural Science Foundation of China (11574223), the Natural Science Foundation of Jiangsu Province (BK20150303) and the Jiangsu Specially-Appointed Professor Program of Jiangsu Province.

- * E-mail: jhu@suda.edu.cn
- ¹ Kane, C. L.; Mele, E. J. Z_2 Topological Order and the Quantum Spin Hall Effect. *Phys. Rev. Lett.*, **2005**, 95, 146802.
- ² Kane, C. L.; Mele, E. J. Quantum Spin Hall Effect in Graphene. *Phys. Rev. Lett.*, **2005**, 95, 226801.
- ³ Bernevig, B. A.; Zhang, S. C. Quantum Spin Hall Effect. *Phys. Rev. Lett.*, **2006**, 96, 106802.
- ⁴ Bernevig, B. A.; Hughes, T. L.; Zhang, S. C. Quantum Spin Hall Effect and Topological Phase Transition in HgTe Quantum Wells. *Science*, **2006**, 314, 1757–1761.
- ⁵ Nagaosa, N. A New State of Quantum Matter. *Science*, **2007**, 318, 758–759.
- ⁶ König, M.; Wiedmann, S.; Brüne, C.; Roth, A.; Buhmann, H.; Molenkamp, L. W.; Qi, X. L.; Zhang, S. C. Quantum Spin Hall Insulator State in HgTe Quantum Wells. *Science*, **2007**, 318, 766–770.
- ⁷ Hasan, M. Z.; Kane, C. L. Colloquium: Topological insulators. *Rev. Mod. Phys.*, **2010**, 82, 3045–3067.
- ⁸ Qi, X. L.; Zhang, S. C. Topological insulators and superconductors. *Rev. Mod. Phys.*, **2011**, 83, 1057–1110.
- ⁹ Weeks, C.; Hu, J.; Alicea, J.; Franz, M.; Wu, R. Q. Engineering a Robust Quantum Spin Hall State in Graphene via Adatom Deposition. *Phys. Rev. X*, **2011**, 1, 021001.
- ¹⁰ Hu, J.; Alicea, J.; Wu, R. Q.; Franz, M. Giant Topological Insulator Gap in Graphene with 5d Adatoms. *Phys. Rev. Lett.*, **2012**, 109, 266801.
- ¹¹ Hu, J.; Zhu, Z. Y.; Wu, R. Q. Chern Half Metals: A New Class of Topological Materials to Realize the Quantum Anomalous Hall Effect. *Nano Lett.*, **2015**, 15, 2074–2078.
- ¹² Liu, C.; Hughes, T. L.; Qi, X. L.; Wang, K.; Zhang, S.-C. Quantum Spin Hall Effect in Inverted Type-II Semiconductors. *Phys. Rev. Lett.*, **2008**, 100, 236601.
- ¹³ Knez, I.; Du, R. R.; Sullivan, G. Evidence for Helical Edge Modes in Inverted InAs/GaSb Quantum Wells. *Phys. Rev. Lett.*, **2011**, 107, 136603.
- ¹⁴ Du, L.; Knez, I.; Sullivan, G.; Du, R. R. Robust Helical Edge Transport in Gated InAs/GaSb Bilayers. *Phys. Rev. Lett.*, **2015**, 114, 096802.
- ¹⁵ Fu, L.; Kane, C. L. Topological insulators with inversion symmetry. *Phys. Rev. B*, **2007**, 76, 045302.
- ¹⁶ Hsieh, D.; Qian, D.; Wray, L.; Xia, Y.; Hor, Y. S.; Cava, R. J.; Hasan, M. Z. A topological Dirac insulator in a quantum spin Hall phase. *Nature*, **2008**, 452, 970–974.
- ¹⁷ Zhang, H. J.; Liu, C. X.; Qi, X. L.; Dai, X.; Fang, Z.; Zhang, S. C. Topological insulators in Bi_2Se_3 , Bi_2Te_3 and Sb_2Te_3 with a single Dirac cone on the surface. *Nat. Phys.*, **2009**, 5, 438–442.
- ¹⁸ Xia, Y.; Qian, D.; Hsieh, D.; Wray, L.; Pal, A.; Lin, H.; Bansil, A.; Grauer, D.; Hor, Y. S.; Cava, R. J.; Hasan, M. Z. Observation of a large-gap topological-insulator class with a single Dirac cone on the surface. *Nat. Phys.*, **2009**, 5, 398–402.
- ¹⁹ Chen, Y. L.; Analytis, J. G.; Chu, J.-H.; Liu, Z. K.; Mo, S.-K.; Qi, X. L.; Zhang, H. J.; Lu, D. H.; Dai, X.; Fang, Z.; Zhang, S. C.; Fisher, I. R.; Hussain, Z.; Shen, Z.-X. Experimental Realization of a Three-Dimensional Topological Insulator, Bi_2Te_3 . *Science*, **2009**, 325, 178–181.
- ²⁰ Weng, H. M.; Dai, X.; Fang, Z. Transition-Metal Pentatelluride ZrTe_5 and HfTe_5 : A Paradigm for Large-Gap Quantum Spin Hall Insulators. *Phys. Rev. X*, **2014**, 4, 011002.

²¹ Chuang, F. C.; Yao, L. Z.; Huang, Z. Q.; Liu, Y. T.; Hsu, C. H.; Das, T.; Lin, H.; Bansil, A. Prediction of Large-Gap Two-Dimensional Topological Insulators Consisting of Bilayers of Group III Elements with Bi. *Nano Lett.*, **2014**, 14, 2505–2508.

²² Ma, Y.; Dai, Y.; Kou, L.; Frauenheim, T.; Heine, T. Robust Two-Dimensional Topological Insulators in Methyl- Functionalized Bismuth, Antimony, and Lead Bilayer Films. *Nano Lett.*, **2015**, 15, 1083–1089.

²³ Li, L. Y.; Zhang, X. M.; Chen, X.; Zhao, M. W. Giant Topological Nontrivial Band Gaps in Chloridized Gallium Bismuthide. *Nano Lett.*, **2015**, 15, 1296–1301.

²⁴ Liu, C. C.; Feng, W. X.; Yao, Y. G. Quantum Spin Hall Effect in Silicene and Two-Dimensional Germanium. *Phys. Rev. Lett.*, **2011**, 107, 076802.

²⁵ Vogt, P.; Padova, P. D.; Quaresima, C.; Avila, J.; Frantzeskakis, E.; Asensio, M. C.; Resta, A.; Ealet, B.; Lay, G. L. Silicene: Compelling Experimental Evidence for Graphenelike Two-Dimensional Silicon. *Phys. Rev. Lett.*, **2012**, 108, 155501.

²⁶ Meng, L.; Wang, Y.; Zhang, L.; Du, S.; Wu, R.; Li, L.; Zhang, Y.; Li, G.; Zhou, H.; Hofer, W. A.; Gao, H. J. Buckled Silicene Formation on Ir(111). *Nano Lett.*, **2013**, 13, 685–690.

²⁷ Wang, Q. H.; Kalantar-Zadeh, K.; Coleman, J. N.; Strano, M. S. Electronics and optoelectronics of two-dimensional transition metal dichalcogenides. *Nat. Nanotech.*, **2012**, 7, 699–712.

²⁸ Chhowalla, M.; Shin, H. S.; Eda, G.; Li, L.-J.; Loh, K. P.; Zhang, H. The chemistry of two-dimensional layered transition metal dichalcogenide nanosheets. *Nat. Chem.*, **2013**, 5, 263–275.

²⁹ Mak, K. F.; Lee, C.; Hone, J.; Shan, J.; Heinz, T. F. Atomically Thin MoS₂: A New Direct-Gap Semiconductor. *Phys. Rev. Lett.*, **2010**, 105, 136805.

³⁰ Liu, K. K.; Zhang, W.; Lee, Y.-H.; Lin, Y.-C.; Chang, M.-T.; Su, C.-Y.; Chang, C.-S.; Li, H.; Shi, Y.; Zhang, H.; Lai C.-S.; Li, L.-J. Growth of Large-Area and Highly Crystalline MoS₂ Thin Layers on Insulating Substrates. *Nano Lett.*, **2012**, 12, 1538–1544.

³¹ Xu, X. D.; Yao, W.; Xiao, D.; Heinz, T. F. Spin and pseudospins in layered transition metal dichalcogenides. *Nat. Phys.*, **2014**, 10, 343–350.

³² Qian, X. F.; Liu, J. W.; Fu, L.; Li, J. Quantum spin Hall effect in two-dimensional transition metal dichalcogenides. *Science*, **2014**, 346, 1344–1347.

³³ Nie, S. M.; Song, Z.; Weng, H. M.; Fang, Z. Quantum spin Hall effect in two-dimensional transition-metal dichalcogenide haeckelites. *Phys. Rev. B*, **2015**, 91, 235434.

³⁴ Hu, J.; Zhang, Y. N.; Law, M.; Wu, R. Q. Increasing the Band Gap of Iron Pyrite by Alloying with Oxygen. *J. Am. Chem. Soc.*, **2012**, 134, 13216.

³⁵ Cheng, Y. C.; Zhu, Z. Y.; Mi, W. B.; Guo, Z. B.; Schwingenschlögl, U. Prediction of two-dimensional diluted magnetic semiconductors: Doped monolayer MoS₂ systems. *Phys. Rev. B*, **2013**, 87, 100401.

³⁶ Kresse, G.; Furthmüller, J. Efficiency of ab-initio total energy calculations for metals and semiconductors using a plane-wave basis set. *Comput. Mater. Sci.*, **1996**, 6, 15–50.

³⁷ Kresse, G.; Furthmüller, J. Efficient iterative schemes for ab initio total-energy calculations using a plane-wave basis set. *Phys. Rev. B*, **1996**, 54, 11169–11186.

³⁸ Blöchl, P. E. Projector augmented-wave method. *Phys. Rev. B*, **1994**, 50, 17953–17979.

³⁹ Kresse, G.; Joubert, D. From ultrasoft pseudopotentials to the projector augmented-wave method. *Phys. Rev. B*, **1999**, 59, 1758–1775.

⁴⁰ Perdew, J. P.; Burke, K.; Ernzerho, M. Generalized Gradient Approximation Made Simple. *Phys. Rev. Lett.*, **1996**, 77, 3865–3868.

⁴¹ Monkhorst, H. J.; Pack, J. D. Special points for Brillouin-zone integrations. *Phys. Rev. B*, **1976**, 13, 5188–5192.

⁴² Fukui, T.; Hatsugai, Y. Quantum spin Hall effect in three dimensional materials: Lattice computation of Z2 topological invariants and its application to Bi and Sb. *J. Phys. Soc. Jpn.*, **2007**, 76, 053702.

⁴³ Xiao, D.; Yao, Y.; Feng, W.; Wen, J.; Zhu, W.; Chen, X. Q.; Stocks, G. M.; Zhang, Z. Half-Heusler Compounds as a New Class of Three-Dimensional Topological Insulators. *Phys. Rev. Lett.*, **2010**, 105, 096404.

⁴⁴ Feng, W.; Wen, J.; Zhou, J.; Xiao, D.; Yao, Y. First-principles calculation of Z2 topological invariants within the FP-LAPW formalism. *Comput. Phys. Commun.*, **2012**, 183, 1849–1859.

⁴⁵ PythTB, by S.Coh and D.Vanderbilt, available at <http://www.physics.rutgers.edu/pythtb/index.html>.

⁴⁶ Marzari, N.; Vanderbilt, D. Maximally localized generalized Wannier functions for composite energy bands. *Phys. Rev. B*, **1997**, 56, 12847.

⁴⁷ Souza, I.; Marzari, N.; Vanderbilt, D. Maximally localized Wannier functions for entangled energy bands. *Phys. Rev. B*, **2001**, 65, 035109.

⁴⁸ , Mostofi, A. A.; Yates, J. R.; Pizzi, G.; Lee, Y. S.; Souza, I.; Vanderbilt, D.; Marzari, N. An updated version of wannier90: A tool for obtaining maximally-localised Wannier functions. *Comput. Phys. Commun.*, **2014**, 185, 2309.

⁴⁹ Ding, Y.; Wang, Y. L.; Ni, J.; Shi, L.; Shi, S. Q.; Tang, W. H. First principles study of structural, vibrational and electronic properties of graphene-like MX₂ (M = Mo, Nb, W, Ta; X = S, Se, Te) monolayers. *Physica B*, **2011**, 406, 2254–2260.

⁵⁰ Wang, G.; Robert, C.; Suslu, A.; Chen, B.; Yang, S.; Alamdari, S.; Gerber, I. C.; Amand, T.; Marie, X.; Tongay S.; Urbaszek, B. Spin-orbit engineering in transition metal dichalcogenide alloy monolayers. *Nat. Commun.*, **2015**, 6, 10110.

⁵¹ Li, H. L.; Yu, K.; Tang, Z.; Zhu, Z. Q. Experimental and First-Principles Investigation of MoWS₂ with High Hydrogen Evolution Performance. *ACS Appl. Mater. Interfaces*, **2016**, 8, 29442–29451.